



Gravitationally lensed quasars in *Gaia* – II. Discovery of 24 lensed quasars

Cameron A. Lemon,^{1,2*} Matthew W. Auger,¹ Richard G. McMahon^{1,2} and Fernanda Ostrovski^{1,2}

¹Institute of Astronomy, University of Cambridge, Madingley Road, Cambridge CB3 0HA, UK

²Kavli Institute for Cosmology, University of Cambridge, Madingley Road, Cambridge CB3 0HA, UK

Accepted 2018 March 23. Received 2018 March 20; in original form 2018 February 13

ABSTRACT

We report the discovery, spectroscopic confirmation, and preliminary characterization of 24 gravitationally lensed quasars identified using *Gaia* observations. Candidates were selected in the Pan-STARRS footprint with quasar-like WISE colours or as photometric quasars from Sloan Digital Sky Survey (SDSS), requiring either multiple detections in *Gaia* or a single *Gaia* detection near a morphological galaxy. The Pan-STARRS *grizY* images were modelled for the most promising candidates and 60 candidate systems were followed up with the William Herschel Telescope. 13 of the lenses were discovered as *Gaia* multiples and 10 as single *Gaia* detections near galaxies. We also discover 1 lens identified through a quasar emission line in an SDSS galaxy spectrum. The lenses have median image separation 2.13 arcsec and the source redshifts range from 1.06 to 3.36. 4 systems are quadruply imaged and 20 are doubly imaged. Deep CFHT data reveal an Einstein ring in one double system. We also report 12 quasar pairs, 10 of which have components at the same redshift and require further follow-up to rule out the lensing hypothesis. We compare the properties of these lenses and other known lenses recovered by our search method to a complete sample of simulated lenses to show the lenses we are missing are mainly those with small separations and higher source redshifts. The initial *Gaia* data release only catalogues all images of ~ 30 per cent of known bright lensed quasars, however the improved completeness of *Gaia* data release 2 will help find all bright lensed quasars on the sky.

Key words: gravitational lensing: strong – methods: observational – quasars: general.

1 INTRODUCTION

There are currently fewer than 40 known gravitationally lensed quasars with image separations over 2 arcsec. The multiple images of these bright wider-separation systems can be monitored to determine time delays, which are used to calculate a time delay distance and hence infer the Hubble constant (Refsdal 1966; Bonvin et al. 2017). This is a promising method to shed light on the apparent tension between local distance measurements (Riess et al. 2016) and CMB measurements (Planck Collaboration XIII 2016). Lensed quasars are also powerful tools to probe the many facets of galaxy evolution: lens mass distributions (Schechter & Wambsganss 2004; Bate et al. 2008, 2011; Mediavilla et al. 2009), source quasar accretion discs (Rauch & Blandford 1991; Pooley et al. 2007; Jiménez-Vicente et al. 2015), source quasar host galaxies (Peng et al. 2006; Bayliss et al. 2017; Ding et al. 2017), etc. However the results of all these studies are currently hindered by the dearth of known lensed quasars.

The first Pan-STARRS data release (Chambers et al. 2016) has provided arcsecond-resolution, multiwavelength (*grizY*) imaging of three-quarters of the sky. This provides the perfect data set to increase the number of bright lensed quasars through area alone. Furthermore the multiwavelength data allow characterization and pre-selection of the most promising candidates to spectroscopically follow up through the use of residual features, goodness of fit, and SED similarity. While many techniques exist for identifying lenses from purely photometric data (Ostrovski et al. 2017; Schechter et al. 2017; Williams et al. 2018), all are plagued by contaminant systems that resemble lensed quasars. These include compact star-forming galaxy pairs, binary quasars, and quasars projected close to blue stars and galaxies. Additionally, the resolution of ground-based imaging data often blends the separate components of lensed quasars into just one catalogued object. This blending by the point spread function (PSF) on the scale of the image separation leads to contaminant systems being confused for lensed quasars. One way to overcome this blending issue is to use the excellent resolution of *Gaia* (Gaia Collaboration 2016a), which is able to separate two point sources separated by ~ 0.1 arcsec (Fabricius et al. 2016). Only a catalogue of detections is currently released from the *Gaia* col-

* E-mail: cl522@ast.cam.ac.uk

laboration (Gaia Collaboration 2016b), however this is enough to quickly reduce the number of contaminants. Even though *Gaia* has not catalogued all components of close pairs (Arenou et al. 2017), the knowledge that a point source exists in a system removes some star-forming galaxy contaminants from the search.

The selection, follow-up, and modelling of lensed quasars using Pan-STARRS and *Gaia* data form the basis of this paper. In Section 2 we describe the search techniques and the starting photometric quasar catalogues. Section 3 explains the observations and their outcomes, and in Section 4 we create light profile and mass models for the systems. Finally we discuss the individual systems and summarize our findings in Sections 5 and 6. Wide-field Infrared Survey Explorer (WISE) magnitudes are quoted in the AB system. The conversions from Vega to AB for ALLWISE data are $W_{1\text{AB}} = W_{1\text{Vega}} + 2.699$ and $W_{2\text{AB}} = W_{2\text{Vega}} + 3.339$, which are given in Jarrett et al. (2011) and in the ALLWISE explanatory supplement. When required, a flat cosmology with $\Omega_m = 0.3$ and $H_0 = 70 \text{ km s}^{-1} \text{ Mpc}^{-1}$ was used.

2 LENS CANDIDATE SELECTION

The following section describes the candidate selection process. The declination range was limited to $\gtrsim -30^\circ$, i.e. requiring *grizY* imaging from Pan-STARRS. For the majority of searches we required the systems to have a galactic latitude, $|b| > 15^\circ$, however in some right ascension ranges ($\text{RA} \sim 80^\circ$, along the galactic anticentre) this was relaxed. Before a final sample was established, the local *Gaia* stellar density for each candidate was required to be less than 50 000 stars per square degree (calculated by counting *Gaia* sources within a 100 arcsec radius), in order to remove star clusters.

Two quasar candidate catalogues are created, and two *Gaia*-based selection methods are applied to these catalogues to generate our final sample, as described in the following subsections.

2.1 Photometric quasar candidate catalogues

2.1.1 I. WISE mid-infrared colours

Stern et al. (2012) have shown that the W1 and W2 bands of WISE (Wright et al. 2010) can be used to select AGN by applying the colour criterion of $W_{1\text{--}W2} \geq 0.16$ (AB). One advantage of this selection technique is its simplicity and effectiveness (Wu et al. 2012; Schechter et al. 2017), however a downside for our purposes is that lensed quasar photometry can be strongly affected by the lensing galaxy, leading to WISE colours bluer than those of isolated quasars.

To overcome this, we apply a looser WISE criterion of $W_{1\text{--}W2} \geq -0.14$. With this limit we do not expect an unreasonable number of contaminants still meeting our *Gaia* detection criteria of Section 2.2. The main contaminant created by this lower limit is quasar+star projections.

We ensure that the WISE detections are robust in W1 and W2 by requiring catalogue uncertainties and a W1 value brighter than 18.2. After matching to Pan-STARRS and keeping objects with *i*-band PSF magnitudes brighter than 21, our initial WISE-selected quasar candidate list has 1298 877 objects with $|b| > 15^\circ$.

2.1.2 II. SDSS GMM photometric quasars

Recent papers (e.g. Agnello et al. 2018a; Williams et al. 2018; Ostrovski in preparation) have shown that the Sloan Digital Sky Survey (SDSS) imaging data still contain bright lensed quasars,

Table 1. Candidate numbers for the two quasar catalogues and the two *Gaia* morphological selection methods.

<i>WISE</i> quasars ($W_{1\text{--}W2} > -0.14$)	1298 877
MULTIPLES	
<i>Gaia</i> matches < 2 arcsec	416 990
2 <i>Gaia</i> matches within 4 arcsec of each other	9125
<i>Gaia</i> astrometric excess noise (AEN) < 10 mas	8889
Stellar density $< 50\,000$ per sq. deg	8447
SINGLES	
<i>Gaia</i> matches < 4 arcsec	428 559
<i>Gaia</i> singles with $r_{\text{PSF}} - r_{\text{KRON}} > 0.2$	120 817
<i>Gaia</i> AEN < 10 mas	80 595
Stellar density $< 50\,000$ per sq. deg	80 206
<i>SDSS GMM</i> quasars	1158 557
MULTIPLES	
<i>Gaia</i> matches < 2 arcsec	686 311
2 <i>Gaia</i> matches within 4 arcsec of each other	24 851
<i>Gaia</i> AEN < 10 mas	24 765
Stellar density $< 50\,000$ per sq. deg	24 749
SINGLES	
<i>Gaia</i> matches < 4 arcsec	710 052
<i>Gaia</i> singles with $r_{\text{PSF}} - r_{\text{KRON}} > 0.2$	54 352
<i>Gaia</i> AEN < 10 mas	50 491
Stellar density $< 50\,000$ per sq. deg	50 488

which had not been targeted for spectroscopy and hence were missed by the SDSS Quasar Lens Search (SQLS; Oguri et al. 2006).

Since the SDSS imaging data set includes *u*-band data – which are particularly useful for selecting AGN – we create a complementary catalogue to the WISE selection above by applying Gaussian mixture modelling (GMM) classification to SDSS objects as in Ostrovski et al. (2018). This is a morphology-independent selection based on *u* – *g*, *g* – *i*, and *i* – W1 colours. Classification is divided into four classes: stars, galaxies, and low- and high-redshift quasars ($z \lesssim 2.7$ and $z \gtrsim 2.7$, respectively). This classification is applied to all SDSS objects with *psfMag_i* < 21 . Our final GMM quasar candidate catalogue is composed of all objects that have a combined (low and high redshift) quasar probability > 0.5 . This results in 1158 557 quasar candidates.

2.2 Morphology selection

Once a set of photometric quasar candidates is selected, we attempt to remove the objects that are not lensed quasars – mainly isolated quasars or misclassified star-forming galaxies. To this end we use *Gaia* data, which have a spatial resolution of $\sim 0.1'$ (Fabricius et al. 2016). *Gaia* is built to detect stars in our galaxy, but naturally detects bright quasars as a by-product. Therefore we search our quasar candidate catalogues for objects in which multiple *Gaia* sources are detected, as would be expected for multiple-imaged quasars. While this does not remove quasar+star projections from our candidates, it removes many star-forming galaxies and isolated quasars, since at most one *Gaia* detection is expected for these contaminants.

Since *Gaia* does not reliably detect all images of most lensed quasars, we also describe a simple morphology selection using just one *Gaia* detection (Lemon et al. 2017). While this selection naturally removes fewer contaminants, it is able to recover 45 known lenses. The details of the two methods are described below. They are both applied to each of the quasar catalogues described in 2.1; Table 1 shows the number of candidates each technique and quasar

catalogue produced, given the selection criteria. Note that the numbers are not exclusive.

2.2.1 Multiple Gaia detections

Our first selection technique is to find quasar candidates with multiple *Gaia* detections. We require at least two *Gaia* detections within 4 arcsec of each other. Lensed quasars with separations above this are very rare (e.g. Oguri & Marshall 2010) and the number of contaminant systems increases roughly proportionally to the maximum image separation allowed in a search. Furthermore *Gaia* is most useful at combating the blending of smaller-separation systems in ground-based optical survey data, in which lenses with images separated by more than 4 arcsec should already be deblended. This technique is applied in a two-step process: first all quasar candidates are matched to *Gaia* within 2 arcsec of the Pan-STARRS detection and secondly this is matched to *Gaia* again within 4 arcsec of the initial *Gaia* position. We choose the first matching distance to be only 2 arcsec since this retains all known lenses with two *Gaia* detections while removing some single quasar candidates projected near stars with *Gaia* detections.

2.2.2 Gaia detection near morphological galaxy

Cross-matching *Gaia* to known lensed quasars (Lemon et al. 2017) demonstrates that only one in five small-separation lensed quasars have all quasar images detected by *Gaia*, even when all images should be detected. Although this fraction increases with separation (one-third at the largest separations; Agnello 2017), requiring multiple *Gaia* detections will miss the majority of lenses. One way to find some of these ‘missing’ lenses is to perform a search depending on only one *Gaia* detection. We do this but require a morphological galaxy within 4 arcsec of the quasar candidate, removing contamination from wider-separation star+quasar projections. If the single *Gaia* detection is indeed a quasar, a bright galaxy within 4 arcsec is a strong candidate for acting as a foreground lens. We crossmatch our quasar candidates to *Gaia* within 4 arcsec and then back to Pan-STARRS within 4 arcsec of our original quasar candidate but requiring the criterion of $r_{PSF} - r_{KRON} > 0.2$ for the new match. This extended object can be the original quasar candidate.

2.3 Final lens candidate catalogue

After applying the *Gaia* multiple and single detection techniques to the two quasar candidate catalogues, we apply two further filters. The first is requiring the astrometric excess noise (AEN; Lindegren et al. 2012, 2016) for each *Gaia* detection to be less than 10 mas. The AEN is a useful indicator for point source/galaxy separation (Belokurov et al. 2016; Koposov, Belokurov & Torrealba 2017) which holds for known lensed quasars (Lemon et al. 2017). Therefore we can remove many star-forming galaxies from our search by applying the simple cut $AEN < 10$ mas. The second filter is removing all candidates with local *Gaia* stellar densities above 50 000 stars per square degree. This is calculated by counting all *Gaia* detections within 100 arcsec.

The catalogues are then stacked and duplicates from the two quasar candidate selection techniques are removed, leaving 109 941 *Gaia* singles and 31 486 *Gaia* pairs. After selecting ~ 200 of the most promising candidates through visual inspection, the Pan-STARRS

grizY images are modelled simultaneously as described in Section 4.1. This is to ensure the postulated quasar images have similar colours and to prioritize systems with residual features consistent with a lensing galaxy.

3 OBSERVATIONS

Spectra of 60 candidates were taken with the Intermediate dispersion Spectrograph and Imaging System (ISIS) on the 4.2-m William Herschel Telescope (WHT) on the nights of 2017 March 31, April 1, September 12 and 13. Since we only needed to identify broad emission line features, we used the low-resolution gratings, R158 ($121 \text{ \AA mm}^{-1}/1.81 \text{ \AA pixel}^{-1}$) for the red arm and B300 ($64 \text{ \AA mm}^{-1}/0.86 \text{ \AA pixel}^{-1}$) for the blue arm. Each lens candidate was positioned along a 1-arcsec-wide slit to capture both quasar images. Multiple position angles were used for one quad candidate, J1721+8842.

After masking cosmic rays and subtracting the sky background, the spectra were visually inspected for broad emission lines in the separated peaks and 1-D spectra were extracted using Gaussian apertures with 0.5 arcsec width.

3.1 Results

Table 2 shows a summary of the observations with sky positions, candidate selection method, outcome of the observation, and WISE and *Gaia* magnitudes.

We have classified 24 objects as lensed quasars since the spectra reveal the presence of (at least) two quasars at the same redshift and the pixel modelling of the Pan-STARRS images reveals a lensing galaxy. Fig. 1 shows Pan-STARRS *gri* cutouts of the confirmed lens systems with *Gaia* detections overlaid. Fig. 2 shows the component spectra for each lens. We are able to establish the lens galaxy redshift for four lenses.

We further discover 10 systems consisting of pairs of quasars at the same redshift, shown in Fig. 3. Their spectra are shown in Fig. 4. However in these systems, the residuals after PSF subtraction do not convincingly demonstrate a lens, or the spectral features rule out the lensing hypothesis. See Section 5.1 for details on individual systems. Summaries of key characteristics of lensed quasars and nearly identical quasars are shown in Tables 3 and 4 respectively.

4 MODELLING

4.1 Pixel modelling

In this section we model the Pan-STARRS *grizY* imaging data for each lens system to derive simple component shapes, positions, and colours. In the next section we use the image and galaxy positions and flux measurements to fit simple lens models to each system.

The PSF is derived by fitting a Moffat profile (Moffat 1969) to a nearby star. The *grizY* Pan-STARRS images are modelled simultaneously with each quasar image fit with a PSF, and galaxies fit with Sérsic profiles (Sérsic 1963) convolved with the PSF. In all lens systems, the presence of a lens galaxy is apparent from the colour image, except for J0630-1201 and J1606-2333. The free parameters for the pixel modelling are the positions of the quasar images and the lensing galaxy, as well as the flattening, size, and Sérsic index of the galaxy, all of which we assume to be the same across bands. The log likelihood is sampled using the EMCEE package Foreman-Mackey et al. (2013) to determine statistical uncertainties. Finally

Table 2. Summary of observations. NIQ=nearly identical quasar, assigned to systems of quasars at the same redshift but without photometric detection of a lensing galaxy. Selection shows the quasar catalogue and *Gaia* technique with which the candidate was selected: S=single, D=double, T=triple. All dates are in 2017. WISE magnitudes and colours are given in the AB system.

Name	RA	Dec.	Selection	W1 – W2, W1	Gaia G	Date, Exp. Time	Outcome
J0003+4555	0.96401	45.92215	D+WISE	0.37, 17.95	17.61, 18.97	12 Sep, 600s	quasar+star
J0011–0845	2.83435	– 8.76407	D+GMM/WISE	0.10, 17.89	20.31, 20.35	12 Sep, 1200s	lens , $z = 1.70$
J0028+0631	7.09369	6.53195	S+GMM/WISE	0.16, 16.86	18.95	12 Sep, 1200s	lens , $z = 1.06$
J0030–1525	7.56378	– 15.41752	S+WISE	–0.09, 17.01	19.30	13 Sep, 1200s	quad lens , $z = 3.36$
J0123–0455	20.84084	– 4.93266	S+GMM/WISE	0.21, 17.28	20.29	12 Sep, 2100s	lens , $z = 1.38$
J0127–1441	21.78539	– 14.68861	D+WISE	0.61, 18.14	20.15, 20.50	12 Sep, 1200s	NIQ, $z = 1.76$
J0139+3526	24.88888	35.43658	D+WISE	0.47, 16.52	19.46, 19.65	12 Sep, 600s	NIQ, $z = 0.65$
J0140–1152	25.01231	– 11.872	S+WISE	0.19, 17.07	18.41	12 Sep, 1800s	lens , $z = 1.80$
J0140+4107	25.20420	41.13331	S+WISE	0.27, 16.82	17.54	12 Sep, 1200s	NIQ, $z = 2.50$
J0146–1133	26.63691	– 11.56113	D+WISE	0.46, 16.87	18.39, 18.66	12 Sep, 1800s	lens , $z = 1.44$
J0232–2429	38.06565	– 24.49433	S+WISE	0.48, 17.14	17.99	13 Sep, 600s	quasar+star
J0235–2433	38.86431	– 24.55356	D+WISE	0.34, 16.70	18.12, 18.85	12 Sep, 1800s	lens , $z = 1.44$
J0259–2338	44.88961	– 23.63388	D+WISE	0.13, 16.91	19.23, 20.34	12 Sep, 2400s	lens , $z = 1.19$
J0322+5024	50.71298	50.41402	D+WISE	0.17, 17.49	18.82, 19.11	12 Sep, 600s	stars
J0417+3325	64.49682	33.41700	S+WISE	0.34, 16.87	19.22	13 Sep, 1200s	lens , $z = 1.41$
J0511–0351	77.91098	– 3.85049	D+WISE	0.57, 18.20	19.25, 19.99	13 Sep, 600s	quasar+other
J0515+0652	78.75772	6.86855	S+WISE	0.35, 18.15	18.98	13 Sep, 1200s	quasar+other
J0616+4912	94.13678	49.20712	S+WISE	0.45, 16.49	18.33	12 Sep, 600s	star+quasar
J0630–1201	97.53796	– 12.02223	T+GMM	0.24, 16.89	19.61, 19.76, 19.95	1 Apr, 1200s	5-image lens , $z = 3.34$
J0659+5217	104.92159	52.28907	D+WISE	0.13, 17.99	18.60, 19.63	12 Sep, 600s	stars
J0723+4739	110.93660	47.65259	S+WISE	0.39, 17.35	19.60	12 Sep, 1200s	inconclusive
J0740+2926	115.05603	29.44677	D+GMM/WISE	0.66, 16.81	18.20, 19.64	12 Sep, 1200s	NIQ, $z = 0.98$
J0812+3349	123.22844	33.83062	S+GMM	0.55, 18.22	19.75	13 Sep, 1500s	NIQ, $z = 1.49$
J0822+6659	125.57509	66.99985	D+GMM/WISE	0.29, 16.75	18.77, 19.20	31 Mar, 900s	stars
J0823+4929	125.87600	49.48748	D+GMM/WISE	0.17, 16.99	19.41, 19.99	1 Apr, 600s	quasar pair, $z = 0.52, 0.86$
J0826+7002	126.53489	70.04488	S+WISE	0.03, 15.90	17.50	13 Sep, 600s	inconclusive, quasar(+star?)
J0840+3550	130.13842	35.83334	S+GMM/WISE	–0.12, 17.21	19.95	31 Mar, 1200s	lens , $z = 1.77$, $z_{\text{lens}} = 0.26$
J0941+0518	145.34378	5.30664	SDSS spectra	–0.05, 16.68	–	31 Mar, 1200s	lens , $z = 1.54$, $z_{\text{lens}} = 0.34$
J0949+4208	147.47830	42.13381	D+GMM/WISE	0.14, 16.72	18.94, 19.81	31 Mar, 1200s	lens , $z = 1.27$, $z_{\text{lens}} = 0.51$
J1139+4143	174.94610	41.73088	D+GMM/WISE	0.32, 18.05	19.46, 19.62	1 Apr, 1200s	NIQ, $z = 2.23$
J1147+3634	176.89300	36.57819	D+GMM	0.79, 18.62	19.16, 20.23	31 Mar, 600s	quasar + star
J1239–2216	189.83645	– 22.27778	S+GMM/WISE	0.61, 17.81	18.28	1 Apr, 750s	quasar + galaxy
J1440+3736	220.20396	37.61107	S+WISE	0.43, 16.91	19.27	1 Apr, 600s	galaxy + star
J1508+3844	227.18253	38.73934	D+GMM/WISE	0.11, 17.28	20.21, 20.92	31 Mar, 2700s	lens , $z = 1.68$
J1536+3629	234.01479	36.49226	S+GMM	–0.36, 19.93	20.51	1 Apr, 600s	galaxy at $z = 0.111$
J1540+4445	235.10759	44.75457	D+GMM/WISE	0.09, 17.37	19.73, 20.37	1 Apr, 600s	NIQ, $z = 0.61$
J1551+3157	237.77584	31.95027	S+GMM/WISE	0.04, 17.41	20.48	31 Mar, 1200s	inconclusive, ($z = 2.27?$)
J1554+2616	238.54871	26.27657	D+GMM/WISE	0.07, 17.88	18.95, 20.03	31 Mar, 600s	quasar + star
J1602+4526	240.70535	45.43528	S+GMM	–0.23, 17.50	20.17	31 Mar, 2700s	lens , $z = 2.16$, $z_{\text{lens}} = 0.43$
J1606–2333	241.50074	– 23.55612	D+WISE	0.64, 16.42	18.74, 18.88	31 Mar, 2400s	quad lens , $z = 1.69$
J1611+5756	242.98266	57.93872	S+GMM/WISE	0.09, 17.74	20.24	31 Mar, 600s	galaxies at $z = 0.257$
J1617–2146	244.25462	– 21.76683	D+WISE	0.65, 18.15	19.75, 20.39	1 Apr, 1500s	inconclusive, likely stars
J1617–2305	244.34009	– 23.09620	D+WISE	0.73, 18.19	18.95, 19.23	13 Sep, 1200s	quasar+star
J1640+1045	250.07549	10.75175	D+GMM/WISE	0.13, 17.02	18.12, 19.87	31 Mar, 3000s	lens , $z = 1.7$
J1709+3828	257.36966	38.46700	D+WISE	–0.01, 17.31	20.07, 20.33	31 Mar, 2650s	lens , $z = 1.38$
J1710+4332	257.74257	43.54287	S+GMM	–0.50, 18.27	20.49	31 Mar, 2100s	lens , $z = 3.08$
J1721+8842	260.45419	88.70621	D+WISE	0.28, 15.65	17.97, 18.24	13 Sep, 4800s	quad lens , $z = 2.37$
J1821+6005	275.37642	60.09062	S+WISE	0.53, 18.20	19.96	13 Sep, 1800s	NIQ, $z = 2.05$
J1831+5447	277.86360	54.79965	D+WISE	0.10, 16.23	18.79, 19.86	12 Sep, 1200s	lens , $z = 1.07$
J2018–3015	304.73256	– 30.26574	T+WISE	0.32, 16.21	18.26, 18.52, 19.72	12 Sep, 900s	stars+galaxy
J2032–2358	308.15741	– 23.97291	D+WISE	0.72, 17.59	19.04, 19.17	13 Sep, 1200s	NIQ, $z = 1.64$
J2057+0217	314.46696	2.29683	D+GMM/WISE	0.81, 18.17	20.06, 20.10	12 Sep, 1200s	NIQ, $z = 1.52$
J2058–0744	314.53051	– 7.74705	D+WISE	0.51, 17.97	19.72, 19.75	13 Sep, 600s	quasar+star
J2111+1349	317.80707	13.82978	S+WISE	0.70, 17.83	19.74	13 Sep, 600s	quasar+star
J2124+1632	321.07029	16.53841	S+GMM/WISE	0.40, 16.48	19.11	12 Sep, 1200s	lens , $z = 1.28$
J2302–2813	345.74028	– 28.22055	S+WISE	0.80, 17.67	18.40	12 Sep, 600s	quasar+star

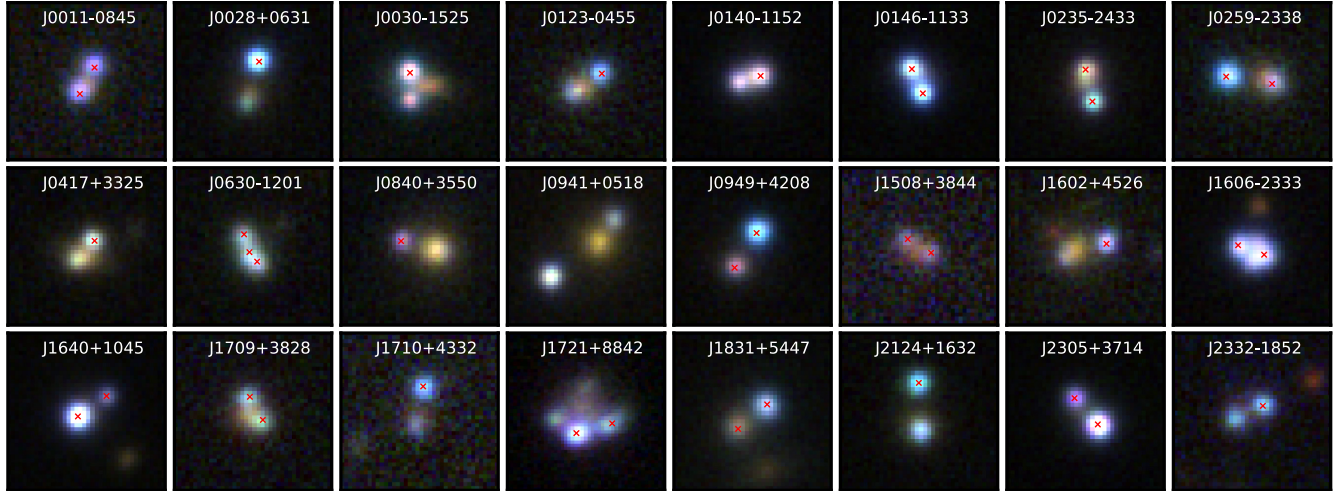
the fitting is repeated with a different PSF star to determine the systematic error for a possible PSF mismatch.

Fig. 5 shows the Pan-STARRS *gri* images and the residuals after modelling each system as the relevant sum of quasars and galaxies.

Astrometry and photometry for all available bands are given in Table A1.

Table 2 – *continued*

Name	RA	Dec.	Selection	$W1 - W2, W1$	<i>Gaia</i> G	Date, Exp. Time	Outcome
J2305+3714	346.48273	37.23932	D+WISE	0.25, 16.35	17.55, 18.71	12 Sep, 1200s	lens , $z = 1.78$
J2327+2238	351.75343	22.63698	D+GMM/WISE	0.12, 17.38	20.68, 20.75	13 Sep, 600s	quasar pair, $z = 0.53, 0.55$
J2332–1852	353.08034	–18.86853	S+WISE	0.32, 17.44	19.48	12 Sep, 1200s	lens , $z = 1.49$
J2350–1930	357.58645	–19.51585	D+WISE	0.50, 18.08	19.49, 20.71	13 Sep, 600s	quasar+star

**Figure 1.** Pan-STARRS *gri* colour images of the confirmed lenses with *Gaia* detections overlaid with red crosses. Cutouts are 10 arcsec on the side.

4.2 Mass modelling

We fit all the systems with singular isothermal ellipsoids (SIE) using our own PYTHON-based image-plane modelling code, which has been checked for consistency with *lensmodel* (Keeton 2001). We use the two-step process of modelling the pixels to find positions and fluxes, and then deriving a lens model. This is to ensure that if the system is not well-described by a singular isothermal ellipsoid, it does not affect the PSF subtraction. Furthermore we can quantify the chi-squared contributions from TAB positions and flux ratios robustly. For all the doubly imaged lenses, we start from two image positions and a galaxy position (six parameters). However, to constrain a singular isothermal ellipsoid (galaxy position, mass, ellipticity, position angle and source position; seven parameters), we require one further observable. For this we use the image flux ratio. We take the median flux ratio from the *griz* bands and include a 20 per cent uncertainty on the input fluxes since optical flux ratios depend not only on the lensing geometry but also on extinction, quasar variability over the time delay, microlensing, etc. Using these pixel-based measurements and their uncertainties, the lens parameters are inferred through image-plane sampling. Given the extra information in quads, we are able to use more realistic models with more parameters. We use SIE+shear models for these systems.

The lens model parameters (medians with 1σ limits) and chi-squared contributions are listed in Table 5. For the three quadruply imaged lenses, we include a 50 per cent uncertainty on the input fluxes for the two saddle point images in each system, in accordance with their increased susceptibility to microlensing (Schechter & Wambsganss 2002).

Systems with significantly elliptical SIE fits and a large image-position chi-squared are indicative of a strong external shear if the lens is not elliptical in the photometry.

5 DISCUSSION

5.1 Notes on individual systems

5.1.1 J0030–1525

The Pan-STARRS *gri* image for this object shows two bright PSFs and a galaxy significantly offset from where it should lie to create a double-image system. However, a better seeing VST *i*-band image (Fig. 6) resolves four objects including a faint blue PSF next to an extended red object. This is consistent with a flux-ratio anomaly fold-configuration quad with the faint PSF being the counterimage. We model the Pan-STARRS data for photometry of A+B, C, and D+G, given in Table A1. However, for the mass model we use the VST *r*-band data given its excellent seeing and resolution of the counterimage. The PSF is inferred from the data due to the lack of a nearby star. We find that the data are fit by models with the merging pair consisting of a bright image north-west of a faint image or vice versa. The former is much more plausible, given that saddle points are more commonly demagnified than maxima and minima (Schechter & Wambsganss 2002) and so this is the mass model we report in Table 5. The best fit mass model gives flux ratios of $\sim 7:7:3:1$ while the measured flux ratios are $\sim 7:0.5:4:1$, i.e. a $14\times$ decrease for image B.

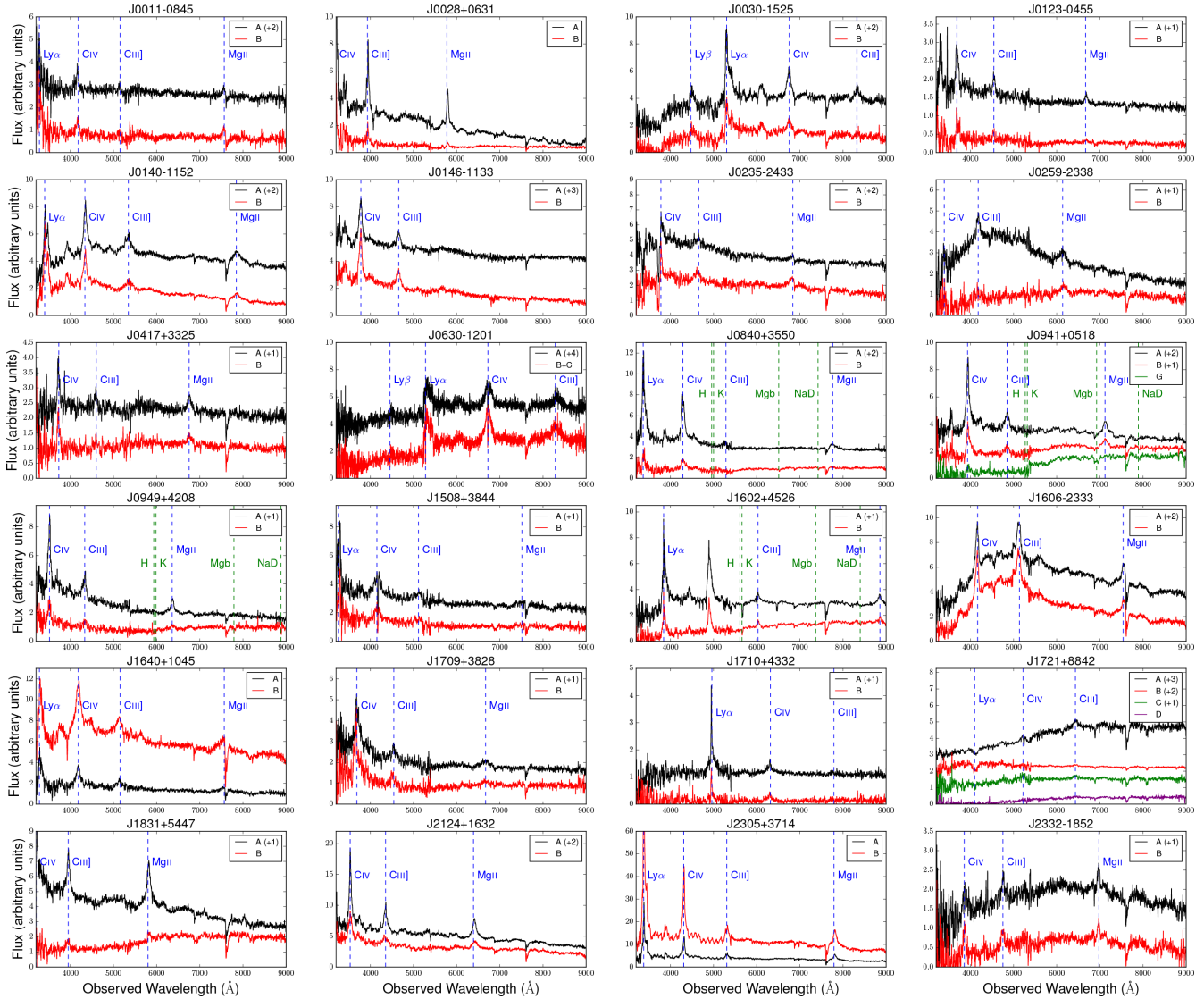


Figure 2. Spectra of the confirmed gravitationally lensed quasars. Quasar emission lines are labelled in blue, and lens galaxy absorption lines in green where identified.

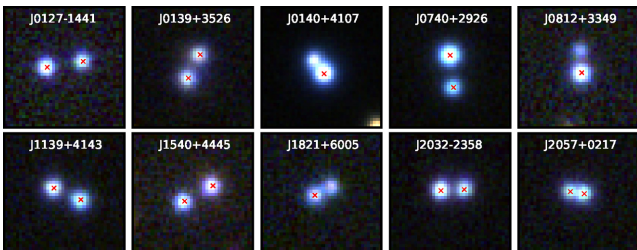


Figure 3. Pan-STARRS *gri* colour images of the nearly identical quasars. Cutouts are 10 arcsec.

5.1.2 *J0127–1441*

DECALS data reveal two faint red objects between the two PSFs that could be responsible for the lensing. These are detected only in the *z*-band data and each has a magnitude of ~ 24 . Comparing to mock lenses from Oguri & Marshall (2010) with similar source redshift and image separation, the faintest *i*-band lens magnitudes are ~ 22 . While the multiple component nature of this putative

lens complicates the comparison, the faintness and large separation suggest either a binary quasar or high-redshift group lens. Deeper data will help to secure the magnitudes of these objects.

5.1.3 *J0139+3526*

While this was a promising candidate given the similar SEDs and residuals consistent with a lensing galaxy, the redshift of the quasars is low ($z = 0.65$) and the [O III] emission lines are significantly different. There is no discernible redshift difference from the spectra, so this system is likely a quasar merger in which we are seeing the onset of AGN activity. The residuals are probably associated with the quasar host galaxies interacting. A nearby bright star makes this system ideal for adaptive optics follow-up.

5.1.4 *J0140-1152*

This lens has been independently identified in the VST-ATLAS survey by Agnello et al. (2018b), who report a lens redshift of

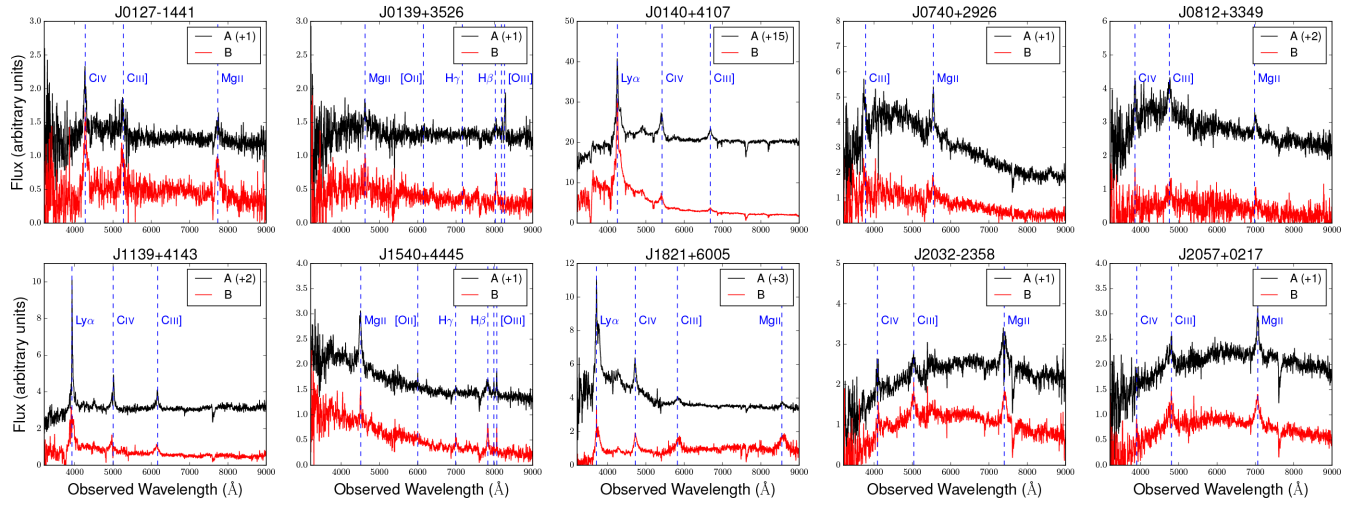


Figure 4. Spectra of the nearly identical quasars and binaries.

Table 3. Summary of lensed quasars (image separations are the largest ones for quads). ^bLens redshift from Agnello et al. (2018b). ^aThese lenses have been independently identified as candidates or confirmed lenses by others as described in Section 5.1.

Name	z_{source}	z_{lens}	Sep. ('')	$i_{\text{images}}, i_{\text{lens}}$
J0011-0845	1.70	–	1.92	20.09, 20.32
J0028+0631	1.06	–	2.78	18.81, 18.44
J0030-1525	3.36	–	1.78	18.60, 18.88
J0123-0455	1.38	–	2.00	19.42, 18.15
J0140-1152 ^a	1.80	0.28 ^b	1.45	18.25, 18.53
J0146-1133 ^a	1.44	–	1.69	18.09, 18.70
J0235-2433 ^a	1.44	–	2.05	18.74, 18.10
J0259-2338 ^a	1.19	–	2.92	19.17, 18.72
J0417+3325	1.41	–	1.59	18.89, 18.54
J0630-1201	3.34	–	1.90	18.30, –
J0840+3550	1.77	0.26	2.46	19.74, 18.03
J0941+0518 ^a	1.54	0.34	5.40	18.30, 17.51
J0949+4208	1.27	0.51	2.57	18.88, 19.19
J1508+3844	1.68	–	1.69	20.67, 20.04
J1602+4526	2.16	0.43	2.70	19.81, 18.67
J1606-2333	1.69	–	1.74	17.58, 20.85
J1640+1045 ^a	1.70	–	2.22	18.24, 18.67
J1709+3828	1.38	–	1.70	19.90, 19.36
J1710+4332	3.08	–	2.43	20.95, 20.60
J1721+8842 ^a	2.37	–	4.03	18.36, 18.02
J1831+5447	1.07	–	2.32	18.80, 18.17
J2124+1632	1.28	–	3.02	18.11, 18.40
J2305+3714	1.78	–	2.20	17.03, 18.32
J2332-1852	1.49	–	1.97	18.76, 18.93

Table 4. Summary of nearly identical quasars and binaries.

Name	z_{source}	Sep. ('')	i_{mag}
J0127-1441	1.76	2.96	19.30
J0139+3526	0.65	2.22	18.49
J0140+4107	2.50	1.44	16.94
J0740+2926	0.98	2.59	18.23
J0812+3349	1.49	1.99	19.12
J1139+4143	2.23	2.30	18.86
J1540+4445	0.61	2.74	19.21
J1821+6005	2.05	1.48	19.34
J2032-2358	1.64	1.91	18.40
J2057+0217	1.52	1.06	18.96

0.277. It is a highly magnified (~ 10 times) double. The elliptical mass model suggests a strong external shear, given the relatively circular light profile of the galaxy.

5.1.5 J0235-2433

Agnello et al. (2017) have independently selected this object as a candidate gravitational lens from the Dark Energy Survey (DES) footprint (The Dark Energy Survey Collaboration 2005). We confirm the PSFs to be quasars at a redshift of 1.44. The DES data displayed in Agnello et al. (2017) show that the image closest to the lens galaxy is brighter than the other while the opposite is true in the Pan-STARRS data. This change by approximately 1 mag within less than a few years (mean epoch for the Pan-STARRS detection is 56475, and ~ 57350 for DES; Abbott et al. 2018) is likely attributed to a microlensing event rather than quasar variability. Indeed in the *Gaia* data, the closest and furthest images have magnitudes of $G=18.12$ and $G=18.85$, respectively. Since both images are detected by *Gaia*, they will have well-sampled light curves over 5 yr. When released, these light curves will clearly distinguish a microlensing event in one image from quasar variability which would be seen in both images but separated by the time delay.

5.1.6 J0417+3325

This double has an elliptical lens galaxy ($q = 0.48$) and the SIE lens model is aligned along the same position angle but less elliptical ($q = 0.65$). It was originally detected by Colla et al. (1970) at 408MHz with a flux of 290 mJy, and subsequently at 5 GHz by Davis (1971) and Altschuler (1986) with detections of 60 mJy and 39 mJy, respectively. It is also detected in NVSS (Condon et al. 1998) at 1.4 GHz with a flux density of 109 mJy. Archival 8 GHz VLA data show two point sources in the same positions as the optical quasar point sources with a hint of a third source south of image A. There is an extended source 3 arcsec west of the system, lacking any optical detection in Pan-STARRS. The A to B flux ratio at 8 GHz is 1.2, while the g -band ratio – the magnitudes least affected by the presence of the lens galaxy – is 2.0, a discrepancy that could be explained by a number of effects including microlensing or extinction. The presence of a radio source is promising for using

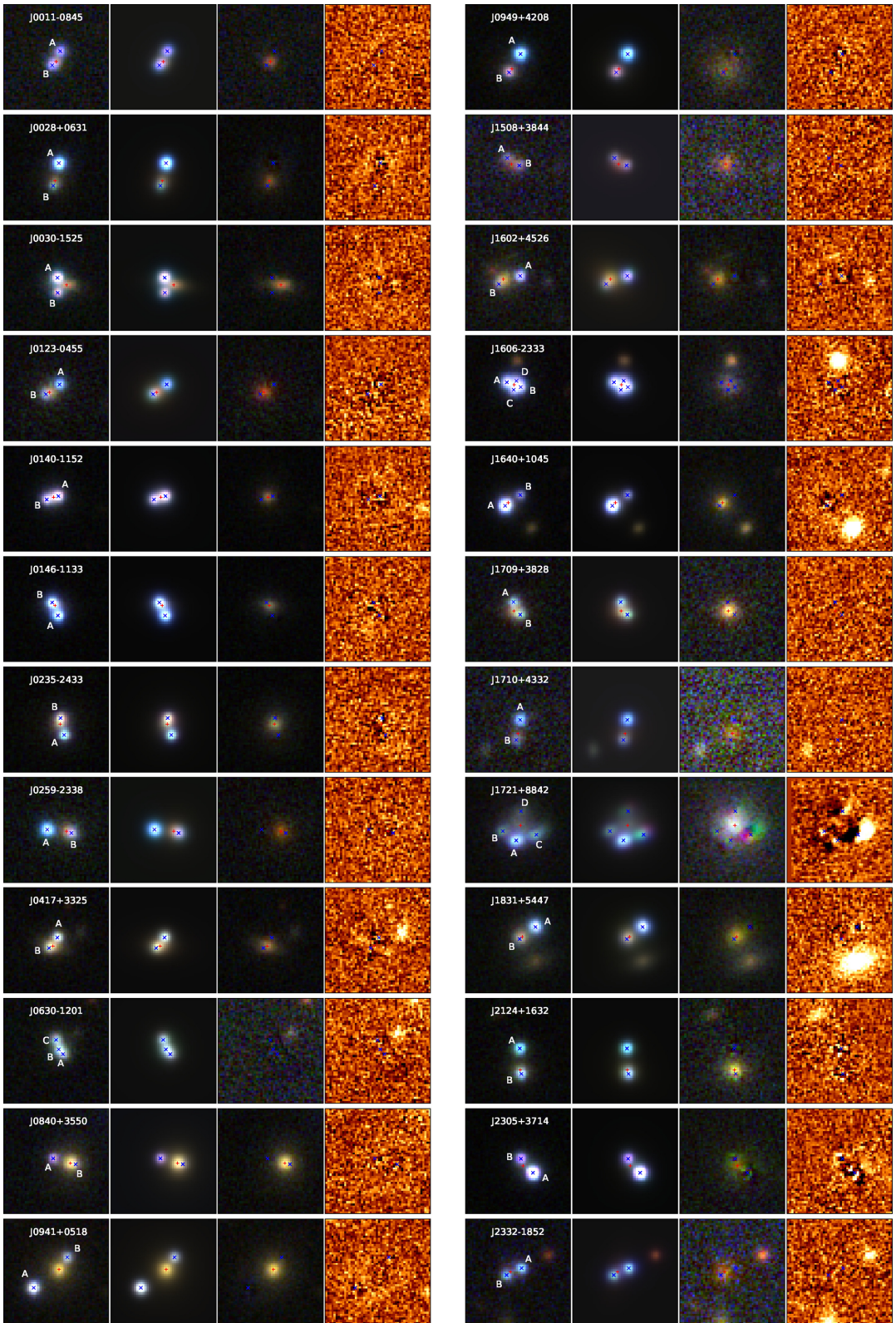


Figure 5. Pixel modelling of the confirmed lenses. Left to right: *gri* data, model, *gri* PSF-subtracted, and *r*-band residuals. Blue crosses indicate the positions of quasar images and red plusses mark the locations of lensing galaxies.

Table 5. Median parameter values with 1σ uncertainties for mass models and light profiles. b=Einstein radius, PA= position angle (north of west), q = axis ratio, μ = total source magnification. ^aThe mass model and galaxy light profile for J0030-1525 are based on better seeing VST-ATLAS data (Shanks et al. 2015) as described in Section 5.1.

name	b ('')	PA_{SIE}	q_{SIE}	PA_{light}	q_{light}	χ^2_{gal}	χ^2_{images}	χ^2_{flux}	μ
J0011-0845	$0.96^{0.97}_{0.95}$	176^{177}_{174}	$0.70^{0.73}_{0.68}$	99^{131}_{55}	$0.86^{0.97}_{0.73}$	0.07	0.19	0.03	$5.0^{5.3}_{4.5}$
J0028+0631	$1.43^{1.44}_{1.42}$	55^{57}_{51}	$0.81^{0.83}_{0.79}$	58^{62}_{54}	$0.86^{0.88}_{0.84}$	0.07	0.19	0.02	$4.2^{4.4}_{4.1}$
J0030-1525 ^a	$1.08^{1.15}_{1.05}$	170^{182}_{165}	$0.82^{0.95}_{0.33}$	55^{57}_{51}	$0.81^{0.83}_{0.79}$	0.97	13.0	13.1	71^{88}_{29}
J0123-0455	$0.96^{0.97}_{0.95}$	136^{140}_{134}	$0.72^{0.75}_{0.68}$	6^{10}_1	$0.84^{0.86}_{0.82}$	0.04	0.09	0.01	$3.5^{3.7}_{3.4}$
J0140-1152	$0.72^{0.73}_{0.71}$	127^{149}_{120}	$0.56^{0.57}_{0.54}$	101^{113}_{94}	$0.92^{0.95}_{0.89}$	0.07	0.18	0.01	$10.3^{11.4}_{9.3}$
J0146-1133	$0.83^{0.84}_{0.82}$	$4.5^{5.4}_{3.4}$	$0.52^{0.58}_{0.45}$	175^{176}_{174}	$0.43^{0.45}_{0.41}$	0.03	0.11	0.01	$3.9^{4.0}_{3.8}$
J0235-2433	$1.04^{1.05}_{1.03}$	44^{45}_{41}	$0.74^{0.75}_{0.73}$	68^{70}_{65}	$0.89^{0.91}_{0.88}$	0.06	0.19	0.02	$5.4^{5.5}_{5.3}$
J0259-2338	$1.41^{1.42}_{1.40}$	99^{101}_{97}	$0.67^{0.70}_{0.65}$	86^{148}_{28}	$0.98^{1.00}_{0.96}$	0.06	0.17	0.04	$3.1^{3.2}_{3.0}$
J0417+3325	$0.82^{0.83}_{0.81}$	173^{175}_{171}	$0.65^{0.68}_{0.64}$	177^{178}_{176}	$0.48^{0.49}_{0.46}$	0.06	0.19	0.01	$4.0^{4.1}_{3.9}$
J0840+3550	$1.43^{1.45}_{1.39}$	164^{166}_{160}	$0.83^{0.88}_{0.79}$	89^{93}_{85}	$0.88^{0.90}_{0.87}$	0.12	0.72	0.39	$4.5^{4.9}_{4.1}$
J0941+0518	$2.72^{2.73}_{2.67}$	97^{109}_{93}	$0.81^{0.82}_{0.77}$	66^{68}_{64}	$0.88^{0.89}_{0.87}$	0.02	0.12	0.01	$5.2^{5.3}_{5.1}$
J0949+4208	$1.23^{1.30}_{1.21}$	155^{157}_{152}	$0.68^{0.76}_{0.62}$	137^{149}_{119}	$0.96^{0.98}_{0.94}$	0.08	0.12	0.02	$3.1^{3.2}_{2.9}$
J1508+3844	$0.92^{0.93}_{0.90}$	103^{107}_{100}	$0.91^{0.93}_{0.88}$	173^{192}_{144}	$0.88^{0.96}_{0.97}$	0.10	0.25	0.03	19^{25}_{15}
J1602+4526	$1.41^{1.44}_{1.40}$	78^{80}_{75}	$0.59^{0.61}_{0.57}$	143^{145}_{140}	$0.74^{0.75}_{0.72}$	0.12	0.19	0.05	$3.4^{3.5}_{3.3}$
J1606-2333	$0.60^{0.61}_{0.59}$	95^{115}_{87}	$0.77^{0.82}_{0.69}$	130^{173}_{104}	$0.67^{0.95}_{0.51}$	0.21	9.9	0.54	$9.4^{10.7}_{8.5}$
J1640+1045	$1.04^{1.05}_{1.03}$	122^{123}_{118}	$0.31^{0.35}_{0.30}$	119^{124}_{114}	$0.88^{0.90}_{0.86}$	0.05	0.07	0.01	$7.6^{8.2}_{5.6}$
J1709+3828	$0.96^{0.97}_{0.95}$	170^{171}_{167}	$0.81^{0.83}_{0.79}$	175^{181}_{170}	$0.81^{0.84}_{0.78}$	0.05	0.06	0.01	$10.7^{11.9}_{9.8}$
J1710+4332	$1.21^{1.23}_{1.20}$	62^{129}_{23}	$0.95^{0.98}_{0.93}$	17^{40}_{-15}	$0.85^{0.96}_{0.72}$	0.03	0.07	0.02	$5.2^{6.1}_{4.6}$
J1721+8842	$1.99^{2.00}_{1.98}$	169^{173}_{146}	$0.87^{0.96}_{0.78}$	136^{139}_{133}	$0.87^{0.88}_{0.86}$	2.55	0.64	1.2	27^{33}_{23}
J1831+5447	$1.10^{1.11}_{1.09}$	126^{130}_{122}	$0.75^{0.79}_{0.71}$	44^{48}_{41}	$0.87^{0.90}_{0.85}$	0.06	0.18	0.02	$3.1^{3.2}_{3.0}$
J2124+1632	$1.41^{1.42}_{1.40}$	176^{177}_{173}	$0.39^{0.50}_{0.34}$	148^{153}_{145}	$0.75^{0.78}_{0.73}$	0.07	0.11	0.01	$2.7^{2.8}_{2.6}$
J2305+3714	$1.10^{1.11}_{1.09}$	59^{62}_{56}	$0.62^{0.67}_{0.60}$	91^{98}_{85}	$0.88^{0.90}_{0.85}$	0.05	0.07	0.01	$8.6^{9.6}_{8.2}$
J2332-1852	$0.96^{0.97}_{0.95}$	99^{101}_{96}	$0.63^{0.67}_{0.59}$	75^{78}_{72}	$0.51^{0.55}_{0.47}$	0.05	0.13	0.01	$4.5^{4.9}_{4.3}$

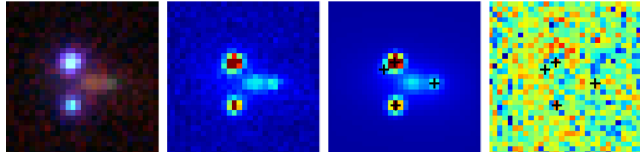


Figure 6. From the left: PSJ0030-1525 VST grz colour image; 0.42-arcsec seeing r -band VST image; 4PSFs+galaxy model with PSF positions overlaid; residuals after model subtraction.

resolved source structure and radio flux ratios to precisely constrain lens models.

5.1.7 J0630-1201

This system was identified in a novel Pan-STARRS+WISE photometric quasar catalogue as explained in Ostrovski et al. (2018). Keck NIRC2 data reveal two lensing galaxies and a fifth demagnified image. See Ostrovski et al. (2018) for a full mass model.

5.1.8 J0740+2926

This is an SDSS quasar that was subsequently found to be followed up as part of the SQLS, which also confirms this as a quasar pair at $z=0.98$ (Inada et al. 2010).

5.1.9 J0812+3349

While we have classified this as a nearly identical quasar (NIQ), there is support for this object being a lens since a faint red object is seen upon subtracting the PSFs. Because of the lack of any imaging data sets other than Pan-STARRS, we cannot confirm this detection since this faint residual is only seen in the i band at $i \sim 23$. The quasars' proximity could mean lens galaxy light is being fit or appearing due to poor PSF subtraction. Therefore deeper and/or higher-resolution imaging of this system is required.

5.1.10 J0941+0518

This system and J1640+1045 were concurrently discovered by Williams et al. (2018). Deep CFHT data reveals an Einstein ring of the quasar host galaxy in the u , g , and r bands, as shown in Fig. 7. We calculate the velocity dispersion of our SIE model to be 365 km s^{-1} and compare this to the measured velocity dispersion of the galaxy from an SDSS spectrum of $313 \pm 18 \text{ km s}^{-1}$. This discrepancy can be accounted for by a shallower than isothermal density profile of $\gamma \sim 1.8$ (see fig. 4 of Auger et al. 2010). However, this lens is embedded within a galaxy group and so close companions would suggest a steeper profile (Dobke, King & Fellhauer 2007; Auger 2008). Since a quasar emission line from the closer, fainter quasar image is present in the galaxy spectrum, the SDSS velocity dispersion might not be trustworthy. A deeper spectrum and deeper optical imaging of the Einstein ring will help constrain the mass

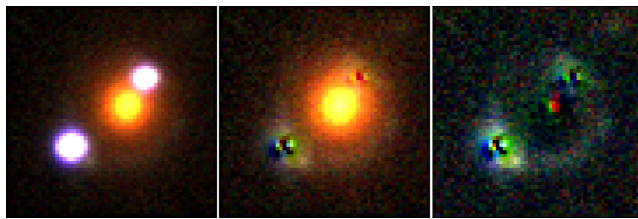


Figure 7. From left to right: J0941+0518 stacked CFHT *ugr* data, PSF-subtraction, and PSF and galaxy subtraction.

model. We calculate the time delay for this system as B lagging A by ~ 270 d.

5.1.11 J0949+4208

This is a radio source in NVSS and FIRST, however FIRST clearly associates it with the lensing galaxy. The lensing galaxy is likely a radio galaxy, however we cannot rule out the fainter optical image being much brighter in the radio. It was targetted for a BOSS spectrum which shows quasar emission lines at $z = 1.27$ and a galaxy at $z = 0.507$, in agreement with the absorption lines seen in our WHT spectrum.

5.1.12 J1540+4445

This NIQ is at low redshift ($z = 0.61$) and shows variation in the emission line profiles between the two components. Furthermore it appears to be associated with a galaxy cluster. Two BOSS spectra of galaxies in the field place them at the same redshift as the NIQ.

5.1.13 J1606–2333

This system was identified as a *Gaia* double. Though the seeing for the WHT spectrum was poor, quasar emission lines are visible across the broad trace. The two-component decomposition is made the same distance as that between the *Gaia* detections, and a narrow uniform aperture is used for the spectral extraction. An archival, shallow *Chandra* image shows extended emission at the positions of the two *Gaia* detections and also near image C, as labelled in Fig. 5. Recent HST imaging (proposal 15320, PI: Treu) clearly resolves four quasar images and a lens galaxy. The mass model suggests a shear of 0.15 and an image position chi-square of ~ 10 . The majority of this is attributed to a poorly fitting position of image D. The best-fit models consistently place D 0.02–0.04 arcsec more northern than the measured value. This discrepancy could be explained by an astrometric perturbation from an unresolved galaxy near image D.

5.1.14 J1640+1045

This double system appears to be a flux-ratio anomaly double with the closest image 1.5 mag brighter than the further image ($0''.52$ and $1''.71$ from the galaxy, respectively). While this could be explained by microlensing, the fit of an SIE is possible to explain this flux ratio but requires a highly elliptical ($q \sim 0.3$) mass model, while the light profile is reasonably circular ($q \sim 0.9$). Therefore if this flux ratio is to be explained by a mass model, it is much more likely to be due to a strong external shear in the same direction as the inferred mass position angle. A singular isothermal sphere + shear model for this system is also a good fit ($\chi^2 \sim 0.25$), with a shear of 0.32

at 122 deg North of East. This position angle is well-aligned with a nearby galaxy less than 4 arcsec from the main lensing galaxy at a position angle of 133 deg North of East. Furthermore SDSS, Pan-STARRS, *Gaia*, and DECaLS data all show that this lens maintains the measured flux ratio implying this flux ratio is unchanging over 15 yr. While microlensing events cannot be ruled out, it is more likely that this apparent flux-ratio anomaly is explained by a strong external shear. Since both quasar images are detected by *Gaia*, their lightcurves will become useful data for breaking the microlensing/shear degeneracy for this system.

5.1.15 J1721+8842

The ‘polar quad’ shows strong signs of line-of-sight absorption systems in all four images. The Pan-STARRS imaging data have highly distorted PSFs in some bands, so the mass model is based on flux ratios measured only in the *r* band. The residuals after subtracting PSFs show flux to the west of image C, perhaps associated with a second lensing galaxy or an arc from the quasar host galaxy. Given its high declination, the position and airmass of this system are essentially unchanged year-round, providing an excellent opportunity to efficiently measure time delays without any seasonal gaps. We note that the mass model is well-fit to the data, with a χ^2 of ~ 4.4 (the number of degrees of freedom for the quad models is $13 - 9 = 4$). Most of the flux chi-squared contribution comes from image A being too bright. This system was also recovered by Rusu et al. (2018) in a lens search using the AGN catalogue of Secret et al. (2015).

5.1.16 J1831+5447

This is an NVSS radio source with a flux of 23.5 mJy at 1.4 GHz.

5.1.17 J2032–2358

MgII absorption is seen in just one of the quasar spectra, with the emission lines appearing similar. The MgII absorption system is at $z = 1.642$, consistent with the source’s systemic redshift based on the C III and C IV lines and the other quasar’s MgII emission line. This could be a lens with magnesium absorption in the host quasar along the line of sight of just one image. If deeper imaging reveals a lens galaxy or a lensed host galaxy, then this system could be used to constrain the covering fraction of MgII.

5.2 Lens statistics

To understand the limitations of our selection method, we have compiled a list of 147 previously known lensed quasars against which we can test our selection. While we report 24 new lensed quasars in this paper, our selection criteria also selected 59 previously known lensed quasars, as described in Table 6.

5.2.1 Recovering known lenses

Of the 171 known lenses (including our sample), 4 lenses have 3 *Gaia* detections, 43 have 2 detections, 86 have 1 detection, and 38 have no detections. Of the 38 with no *Gaia* detections, only 2 have bright enough images that should be detectable by *Gaia* – J0941+0518 and WFI2026-4536 – with the rest being optically faint mainly due to radio selection.

Table 6. *Gaia* selection of lenses with WISE+GMM colour techniques. Numbers shown in brackets are for lenses in the Pan-STARRS footprint. 82 lenses are selected in Pan-STARRS, 23 of which are new lenses presented in this paper and the remaining 59 are known lenses.

Known lensed quasars (in PS)	171 (150)
3 <i>Gaia</i> detections (in PS)	4 (4)
2 <i>Gaia</i> detections ^a (in PS)	43 (34)
1 <i>Gaia</i> detections (in PS)	86 (77)
0 <i>Gaia</i> detections (in PS)	38 (35)
Multiples selected by WISE or GMM in PS	37
Singles selected by WISE or GMM in PS	45

^aOne of these 43 lenses – SBS1520+530 – has one of its two detections due to a nearby star. We keep this in our sample since it would still be selected via this method.

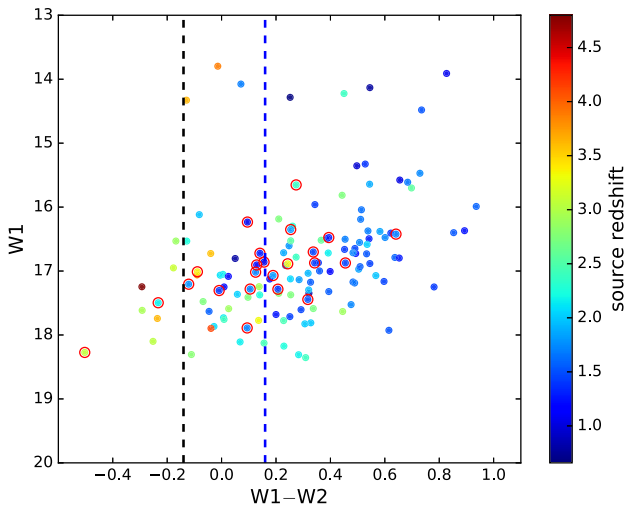


Figure 8. W_1 against $W_1 - W_2$ for all known lenses with at least one *Gaia* detection and robust WISE photometry, coloured by source redshift. Our *Gaia* samples are circled. Lenses circled to the left of the $W_1 - W_2 = -0.14$ black dashed line were selected with the GMM method only. The blue dashed line shows the quasar selection criterion of Stern et al. (2012).

Applying our selection criteria (Section 2), we recover 82 lenses (37 *Gaia* multiples and 45 *Gaia* singles). 23 of these lenses are quadruply imaged (quad fraction of 28 per cent), while of all known lenses the quad fraction is 43/171 (25 per cent). The lenses that we fail to select fall into three categories: separation > 4 arcsec, separation ~ 1 arcsec, or high flux ratio doubles. We do not recover the very rare large-separation lenses because of our 4 arcsec *Gaia* multiple separation cut. The small-separation lenses are missed because of lack of multiple *Gaia* detections (see Lemon et al. 2017), and in the case of just one *Gaia* detection, the system is not extended enough and does not pass our morphological classifier. This latter failure also explains the high flux ratio doubles being missed, since the majority of the flux is in one PSF.

5.2.2 Known versus simulated lenses

Our search techniques failed to recover 33 known lenses with *Gaia* detections. We understand this as the extremes of small- and high-separation images and high flux-ratio doubles. We can verify this and infer which lenses our search is missing by comparing the selected lenses to a simulated sample.

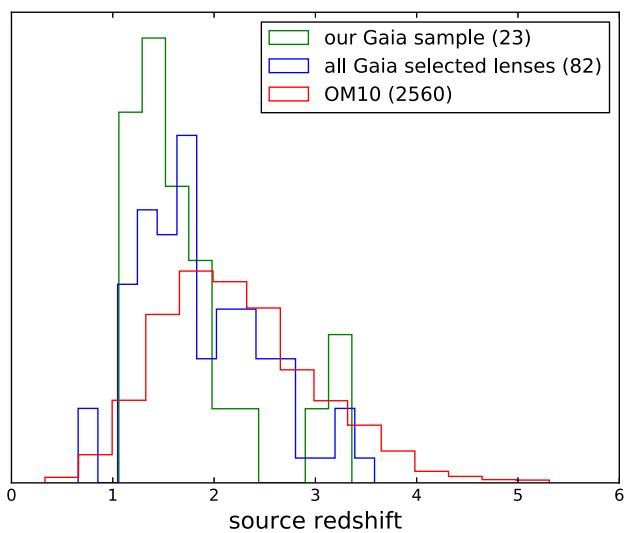


Figure 9. Source redshift distributions for our *Gaia* sample, all *Gaia*-selected lenses, and OM10 mock lenses.

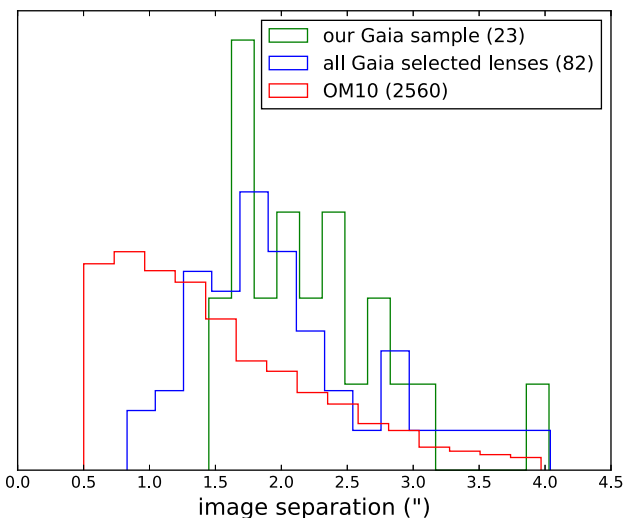


Figure 10. Image separation distributions for our *Gaia* sample, all *Gaia*-selected lenses, and OM10 mock lenses. OM10 used a lower limit of $0.5''$ for the image separation of their mocks and 4 arcsec as an upper limit.

In particular, we compare to the Oguri & Marshall (2010) (OM10 hereafter) simulations which have readily listed image configurations, lensing galaxy parameters, source parameters etc., for 15 658 mock systems. We limit the entire OM10 sample to those lenses we would expect to be able to find with images brighter than the *Gaia* threshold. For this criterion we use all lenses that have the faintest image (or second faintest for quads) brighter than $i = 21$, leaving a catalogue of 2560 mock lenses.

Figs 9 and 10 show histograms of source redshifts and separations, respectively, for our 23 *Gaia* lens sample, the 82 *Gaia*-selected known lenses and the reduced OM10 sample. The first plot demonstrates the lack of known lenses at redshifts above $z = 2.2$. Two reasons for this are (i) SQLS targeted lenses below this redshift for their statistical sample and (ii) the u -band dropout for quasars above $z = 2.7$ makes them more difficult to classify, and at higher redshifts WISE colours tend to become bluer for quasars (as in Fig. 8). The second plot shows that small-separation lenses are being missed.

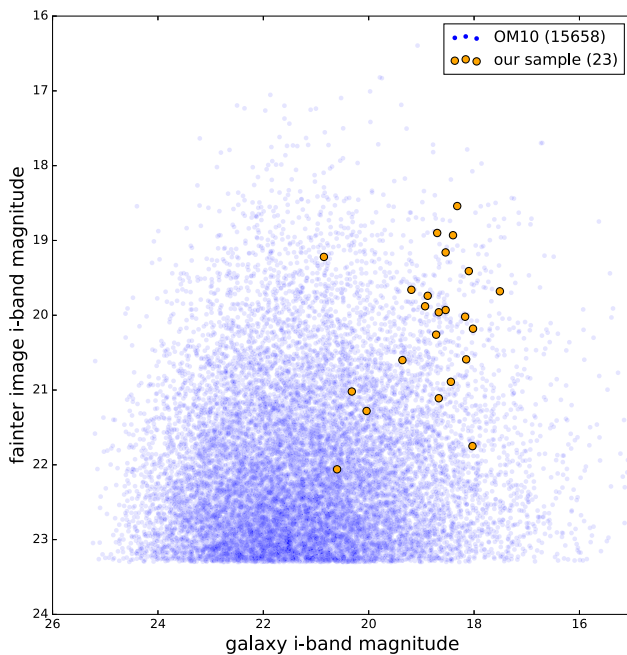


Figure 11. Fainter image (second faintest for quads) magnitudes against lensing galaxy magnitudes in the i band. Yellow dots are from our modelled sample and blue is the entire OM10 simulations (no brightness limit).

This is naturally expected since these are the hardest to identify in imaging data and to target for follow-up spectroscopy.

We note that the quad fraction of the mocks is 18 per cent, compared to 25 per cent for all known lenses, demonstrating current and previous search biases towards quads – they are more identifiable once visually inspected and more likely to be caught by search algorithms (e.g. higher likelihood of multiple *Gaia* detections).

Fig. 11 shows the fainter image magnitude against galaxy magnitude in the i band for our *Gaia* lens sample. Overlaid are the same values for the entire OM10 mock catalogue. Naturally we are still discovering the brightest lenses on the sky, but we note that there should be many more lenses with bright images with faint galaxies, and faint images with bright galaxies (the top left and the bottom right, respectively). The NIQs identified in this paper can make up the former of these two classes of lens, but require deeper imaging to reveal the lens galaxy. The latter will be missed by searches requiring quasar colour selection. These lenses could be discovered by starting from photometric galaxies and requiring multiple *Gaia* detections, as Lucey et al. (2017) have successfully applied to the Pan-STARRS data set.

6 CONCLUSIONS

We have presented the discovery of 24 gravitationally lensed quasars; 13 are discovered by having multiple *Gaia* components, 10 as *Gaia* detections near morphological galaxies, and 1 from an emission line identification in an SDSS galaxy spectrum. All of these systems have well-resolved images in ground-based imaging and are bright, lending themselves to monitoring and subsequent time delay cosmography studies (Treu & Marshall 2016). Our sample includes four quadruply imaged lenses and one double lens which shows a blue Einstein ring in deep CFHT data. One quad, J0030-1525, requires high-resolution imaging to verify our understanding that one image is highly demagnified, by a factor of ~ 14 . Four of our lenses – J0140-1152, J0146-1133, J0235-2433, and J0259-2338

– have been independently identified using a complementary *Gaia* and WISE selection by Agnello et al. (2018b) and Agnello et al. (2017).

Comparing our sample of lensed quasars to simulations, we show that we are not sensitive to arcsecond-separation lenses and those at redshifts beyond the u -band dropout. This is due to colour selection and the bias from visually inspecting a large number of candidates. This biases our sample towards systems with bright lensing galaxies and quads, and away from small-separation lenses and bright doubles that are often confused for stars. The second *Gaia* data release on 2018 April 25 will not only help increase the completeness of lens searches through detection of more lensed quasar images and colour information from the blue and red photometers, but also drastically reduce the number of candidates that must be inspected. Further data release, including proper motion information, will further remove contaminants.

Oguri & Marshall (2010) predict several thousand lensed quasars to be detectable using LSST (Large Synoptic Survey Telescope), however to confirm such large numbers of lenses to become useful astrophysical and cosmological tools, we must ensure we select lenses efficiently and in a complete manner. We have demonstrated that combining *Gaia*, WISE, SDSS, and Pan-STARRS data with pixel-based modelling can efficiently select new lenses – a 57 per cent success rate (including binaries).

ACKNOWLEDGEMENTS

CAL and RGM would like to thank the STFC, and MWA acknowledges support from the STFC in the form of an Ernest Rutherford Fellowship. This work has made use of data from the European Space Agency (ESA) mission *Gaia* (<https://www.cosmos.esa.int/gaia>), processed by the *Gaia* Data Processing and Analysis Consortium (DPAC, <https://www.cosmos.esa.int/web/gaia/dpac/consortium>). Funding for the DPAC has been provided by national institutions, in particular the institutions participating in the *Gaia* Multilateral Agreement. The Pan-STARRS1 Surveys (PS1) and the PS1 public science archive have been made possible through contributions by the Institute for Astronomy, the University of Hawaii, the Pan-STARRS Project Office, the Max-Planck Society and its participating institutes, the Max Planck Institute for Astronomy, Heidelberg, and the Max Planck Institute for Extraterrestrial Physics, Garching, The Johns Hopkins University, Durham University, the University of Edinburgh, the Queen's University Belfast, the Harvard-Smithsonian Center for Astrophysics, the Las Cumbres Observatory Global Telescope Network Incorporated, the National Central University of Taiwan, the Space Telescope Science Institute, the National Aeronautics and Space Administration under Grant No. NNX08AR22G issued through the Planetary Science Division of the NASA Science Mission Directorate, the National Science Foundation Grant No. AST-1238877, the University of Maryland, Eotvos Lorand University (ELTE), the Los Alamos National Laboratory, and the Gordon and Betty Moore Foundation. This publication makes use of data products from the Wide-field Infrared Survey Explorer, which is a joint project of the University of California, Los Angeles, and the Jet Propulsion Laboratory/California Institute of Technology, funded by the National Aeronautics and Space Administration.

REFERENCES

- Abbott T. M. C. et al., 2018, preprint ([arXiv:1801.03181](https://arxiv.org/abs/1801.03181))
- Agnello A., 2017, *MNRAS*, 471, 2013

- Agnello A. et al., 2017, preprint ([arXiv:1711.03971](https://arxiv.org/abs/1711.03971))
- Agnello A., Grillo C., Jones T., Treu T., Bonamigo M., Suyu S. H., 2018a, *MNRAS*, 474, 3391
- Agnello A. et al., 2018b, *MNRAS*, 475, 2086
- Altschuler D. R., 1986, *A&AS*, 65, 267
- Arenou F. et al., 2017, preprint ([arXiv:1701.00292](https://arxiv.org/abs/1701.00292))
- Auger M. W., 2008, *MNRAS*, 383, L40
- Auger M. W., Treu T., Bolton A. S., Gavazzi R., Koopmans L. V. E., Marshall P. J., Moustakas L. A., Burles S., 2010, *ApJ*, 724, 511
- Bate N. F., Floyd D. J. E., Webster R. L., Wyithe J. S. B., 2008, *MNRAS*, 391, 1955
- Bate N. F., Floyd D. J. E., Webster R. L., Wyithe J. S. B., 2011, *ApJ*, 731, 71
- Bayliss M. B. et al., 2017, preprint ([arXiv:1708.00453](https://arxiv.org/abs/1708.00453))
- Belokurov V., Erkal D., Deason A. J., Koposov S. E., De Angeli F., Wyn Evans D., Fraternali F., Mackey D., 2016, *MNRAS*
- Bonvin V. et al., 2017, *MNRAS*, 465, 4914
- Chambers K. C. et al., 2016, preprint ([arXiv:1612.05560](https://arxiv.org/abs/1612.05560))
- Colla G. et al., 1970, *A&AS*, 1, 281
- Condon J. J., Cotton W. D., Greisen E. W., Yin Q. F., Perley R. A., Taylor G. B., Broderick J. J., 1998, *AJ*, 115, 1693
- Davis M. M., 1971, *AJ*, 76, 980
- Ding X. et al., 2017, preprint ([arXiv:1703.02041](https://arxiv.org/abs/1703.02041))
- Dobke B. M., King L. J., Fellhauer M., 2007, *MNRAS*, 377, 1503
- Fabricius C. et al., 2016, *A&A*, 595, A3
- Foreman-Mackey D., Hogg D. W., Lang D., Goodman J., 2013, *PASP*, 125, 306
- Gaia Collaboration, 2016a, *A&A*, 595, A1
- Gaia Collaboration, 2016b, *A&A*, 595, A2
- Inada N. et al., 2010, *AJ*, 140, 403
- Jarrett T. H. et al., 2011, *ApJ*, 735, 112
- Jiménez-Vicente J., Mediavilla E., Kochanek C. S., Muñoz J. A., 2015, *ApJ*, 799, 149
- Keeton C. R., 2001, preprint ([arXiv:astro-ph/](https://arxiv.org/abs/astro-ph/))
- Koposov S. E., Belokurov V., Torrealba G., 2017, preprint ([arXiv:1702.01122](https://arxiv.org/abs/1702.01122))
- Lemon C. A., Auger M. W., McMahon R. G., Koposov S. E., 2017, *MNRAS*, 472, 5023
- Lindgren L., Lammers U., Hobbs D., O'Mullane W., Bastian U., Hernández J., 2012, *A&A*, 538, A78
- Lindgren L. et al., 2016, *A&A*, 595, A4
- Lucey J. R., Schechter P. L., Smith R. J., Anguita T., 2017, preprint ([arXiv:1711.02674](https://arxiv.org/abs/1711.02674))
- Mediavilla E. et al., 2009, *ApJ*, 706, 1451
- Moffat A. F. J., 1969, *A&A*, 3, 455
- Oguri M., Marshall P. J., 2010, *MNRAS*, 405, 2579
- Oguri M. et al., 2006, *AJ*, 132, 999
- Ostrovski F. et al., 2017, *MNRAS*, 465, 4325
- Ostrovski F. et al., 2018, *MNRAS*, 473, L116
- Peng C. Y., Impey C. D., Rix H.-W., Kochanek C. S., Keeton C. R., Falco E. E., Lehár J., McLeod B. A., 2006, *ApJ*, 649, 616
- Planck Collaboration et al., 2016, *A&A*, 594, A13
- Pooley D., Blackburne J. A., Rappaport S., Schechter P. L., 2007, *ApJ*, 661, 19
- Rauch K. P., Blandford R. D., 1991, *ApJ*, 381, L39
- Refsdal S., 1966, *MNRAS*, 132, 101
- Riess A. G. et al., 2016, *ApJ*, 826, 56
- Rusu C. E., Berghea C. T., Fassnacht C. D., More A., Seman E., Nelson G. J., 2018, preprint ([arXiv:1803.07175](https://arxiv.org/abs/1803.07175))
- Schechter P. L., Wambsganss J., 2002, *ApJ*, 580, 685
- Schechter P. L., Wambsganss J., 2004, in Ryder S., Pisano D., Walker M., Freeman K., eds, IAU Symposium Vol. 220, Dark Matter in Galaxies. p. 103 ([arXiv:astro-ph/0309163](https://arxiv.org/abs/astro-ph/0309163))
- Schechter P. L., Morgan N. D., Chehade B., Metcalfe N., Shanks T., McDonald M., 2017, *AJ*, 153, 219
- Secrest N. J., Dudik R. P., Dorland B. N., Zacharias N., Makarov V., Fey A., Frouard J., Finch C., 2015, *ApJS*, 221, 12
- Sérsic J. L., 1963, Bol. Soc. Argent. Astron. Plata Argent., 6, 41
- Shanks T. et al., 2015, *MNRAS*, 451, 4238
- Stern D. et al., 2012, *ApJ*, 753, 30
- The Dark Energy Survey Collaboration 2005, ([arXiv:astro-ph/](https://arxiv.org/abs/astro-ph/)),
- Treu T., Marshall P. J., 2016, *A&A Rev.*, 24, 11
- Williams P. R. et al., 2018, *MNRAS*, p. sly043
- Wright E. L. et al., 2010, *AJ*, 140, 1868
- Wu X.-B., Hao G., Jia Z., Zhang Y., Peng N., 2012, *AJ*, 144, 49

APPENDIX A:

Table A1. Pan-STARRS astrometry and photometry of the lensed quasars. Magnitudes are in the AB system.

	Component	α ('')	δ ('')	<i>g</i>	<i>r</i>	<i>i</i>	<i>z</i>	<i>Y</i>
J0011–0845	A	0.46 ± 0.02	1.24 ± 0.01	20.90 ± 0.01	20.67 ± 0.01	20.69 ± 0.01	20.64 ± 0.03	20.78 ± 0.05
	B	−0.48 ± 0.10	−0.44 ± 0.10	21.03 ± 0.02	20.78 ± 0.06	21.02 ± 0.09	20.41 ± 0.23	20.52 ± 0.14
	G	0.00 ± 0.05	0.00 ± 0.04	22.71 ± 0.22	20.85 ± 0.12	20.32 ± 0.09	20.03 ± 0.15	19.89 ± 0.17
J0028+0631	A	0.44 ± 0.01	2.09 ± 0.01	18.82 ± 0.01	18.75 ± 0.01	18.98 ± 0.01	19.23 ± 0.01	19.11 ± 0.02
	B	−0.23 ± 0.01	−0.59 ± 0.10	20.65 ± 0.01	20.39 ± 0.02	20.89 ± 0.04	21.07 ± 0.07	20.73 ± 0.07
	G	0.00 ± 0.01	0.00 ± 0.01	20.23 ± 0.02	19.11 ± 0.12	18.44 ± 0.01	18.19 ± 0.01	18.00 ± 0.02
J0030–1525	A	−1.09 ± 0.01	0.86 ± 0.01	19.54 ± 0.01	19.22 ± 0.01	19.07 ± 0.01	18.86 ± 0.01	18.87 ± 0.01
	B	−1.05 ± 0.19	−0.92 ± 0.01	20.11 ± 0.01	19.78 ± 0.01	19.74 ± 0.01	19.66 ± 0.01	19.89 ± 0.02
	G	0.00 ± 0.09	0.0 ± 0.09	20.58 ± 0.02	19.34 ± 0.012	18.88 ± 0.01	18.53 ± 0.01	18.37 ± 0.02
J0123–0455	A	1.20 ± 0.01	0.93 ± 0.01	19.08 ± 0.01	19.11 ± 0.01	19.87 ± 0.01	19.67 ± 0.01	20.06 ± 0.03
	B	−0.43 ± 0.01	−0.25 ± 0.01	19.77 ± 0.01	19.47 ± 0.02	20.59 ± 0.07	19.98 ± 0.07	20.46 ± 0.24
	G	0.00 ± 0.01	0.00 ± 0.01	20.28 ± 0.04	19.12 ± 0.03	18.15 ± 0.02	18.17 ± 0.02	17.80 ± 0.03
J0140–1152	A	0.57 ± 0.01	0.11 ± 0.01	19.54 ± 0.01	19.08 ± 0.01	18.87 ± 0.01	19.09 ± 0.01	18.92 ± 0.02
	B	−0.81 ± 0.01	−0.30 ± 0.01	19.62 ± 0.01	19.30 ± 0.01	19.16 ± 0.01	19.23 ± 0.01	19.16 ± 0.02
	G	0.00 ± 0.02	0.00 ± 0.01	20.18 ± 0.02	18.92 ± 0.02	18.53 ± 0.01	18.38 ± 0.03	17.87 ± 0.02
J0146–1133	A	0.34 ± 0.01	−1.20 ± 0.01	18.91 ± 0.01	18.74 ± 0.01	18.79 ± 0.01	18.74 ± 0.01	18.83 ± 0.01
	B	−0.35 ± 0.01	0.33 ± 0.01	19.17 ± 0.01	18.85 ± 0.01	18.90 ± 0.01	18.83 ± 0.01	19.12 ± 0.03
	G	0.00 ± 0.01	0.00 ± 0.01	20.32 ± 0.03	19.30 ± 0.02	18.70 ± 0.02	18.52 ± 0.02	18.24 ± 0.02
J0235–2433	A	0.48 ± 0.01	−1.30 ± 0.01	19.73 ± 0.02	19.47 ± 0.02	19.58 ± 0.02	19.90 ± 0.03	19.66 ± 0.05
	B	0.06 ± 0.01	0.71 ± 0.01	20.24 ± 0.03	19.93 ± 0.02	19.41 ± 0.02	20.16 ± 0.03	19.55 ± 0.07
	G	0.00 ± 0.01	0.00 ± 0.01	19.43 ± 0.03	18.43 ± 0.02	18.10 ± 0.01	17.92 ± 0.01	17.59 ± 0.02
J0259–2338	A	−2.29 ± 0.01	0.19 ± 0.01	19.09 ± 0.02	19.00 ± 0.02	19.66 ± 0.02	19.20 ± 0.02	19.06 ± 0.09
	B	0.59 ± 0.01	−0.22 ± 0.01	19.83 ± 0.03	19.79 ± 0.04	20.26 ± 0.03	20.06 ± 0.05	19.58 ± 0.13
	G	0.00 ± 0.01	0.00 ± 0.01	21.69 ± 0.25	19.44 ± 0.04	18.72 ± 0.02	18.13 ± 0.02	18.15 ± 0.05
J0417+3325	A	0.54 ± 0.01	1.01 ± 0.02	20.35 ± 0.01	19.64 ± 0.01	19.41 ± 0.01	19.14 ± 0.01	19.04 ± 0.01
	B	−0.46 ± 0.01	−0.23 ± 0.01	21.10 ± 0.02	20.22 ± 0.02	19.93 ± 0.03	19.59 ± 0.03	19.39 ± 0.04
	G	0.00 ± 0.01	0.00 ± 0.01	20.58 ± 0.02	19.33 ± 0.01	18.54 ± 0.01	18.07 ± 0.02	17.93 ± 0.02
J0630–1201	A	0.0 ± 0.01	0.00 ± 0.01	20.50 ± 0.01	19.69 ± 0.01	19.60 ± 0.01	19.12 ± 0.01	19.14 ± 0.02
	B	0.53 ± 0.01	−0.58 ± 0.01	20.58 ± 0.02	19.86 ± 0.02	19.44 ± 0.01	19.18 ± 0.02	19.12 ± 0.02
	C	−0.31 ± 0.01	1.13 ± 0.01	20.48 ± 0.01	19.65 ± 0.01	19.44 ± 0.01	19.16 ± 0.01	19.05 ± 0.01
J0840+3550	A	−2.04 ± 0.01	0.56 ± 0.01	20.38 ± 0.01	20.58 ± 0.01	19.92 ± 0.01	19.99 ± 0.01	20.34 ± 0.01
	B	0.64 ± 0.04	−0.14 ± 0.03	21.59 ± 0.05	22.06 ± 0.15	21.75 ± 0.20	21.96 ± 0.23	22.43 ± 0.48
	G	0.00 ± 0.02	0.00 ± 0.01	19.48 ± 0.02	18.54 ± 0.01	18.03 ± 0.01	17.69 ± 0.01	17.65 ± 0.01
J0941+0518	A	−3.02 ± 0.01	−2.18 ± 0.01	19.39 ± 0.01	18.96 ± 0.01	18.66 ± 0.01	18.85 ± 0.01	18.76 ± 0.01
	B	0.97 ± 0.01	1.46 ± 0.01	20.16 ± 0.01	19.93 ± 0.01	19.68 ± 0.01	19.86 ± 0.01	19.65 ± 0.02
	G	0.0 ± 0.01	0.00 ± 0.01	19.43 ± 0.01	18.08 ± 0.01	17.51 ± 0.01	17.16 ± 0.01	16.85 ± 0.01
J0949+4208	A	1.04 ± 0.01	1.77 ± 0.09	19.10 ± 0.02	19.02 ± 0.01	19.61 ± 0.03	19.53 ± 0.02	19.75 ± 0.04
	B	−0.31 ± 0.01	−0.42 ± 0.01	20.19 ± 0.02	19.99 ± 0.02	19.66 ± 0.02	19.90 ± 0.03	19.97 ± 0.05
	G	0.00 ± 0.02	0.00 ± 0.04	20.87 ± 0.12	19.59 ± 0.04	19.19 ± 0.05	18.54 ± 0.02	18.45 ± 0.04
J1508+3844	A	−0.50 ± 0.03	0.70 ± 0.03	22.18 ± 0.02	21.95 ± 0.04	21.58 ± 0.06	21.27 ± 0.07	21.09 ± 0.12
	B	0.96 ± 0.03	−0.19 ± 0.03	22.14 ± 0.02	21.79 ± 0.03	21.28 ± 0.05	20.93 ± 0.04	21.38 ± 0.11
	G	0.00 ± 0.04	0.00 ± 0.05	22.47 ± 0.10	21.22 ± 0.05	20.04 ± 0.05	19.72 ± 0.04	19.39 ± 0.05
J1602+4526	A	1.99 ± 0.01	0.38 ± 0.01	19.99 ± 0.01	20.39 ± 0.01	20.20 ± 0.01	19.92 ± 0.01	20.05 ± 0.01
	B	−0.52 ± 0.02	−0.60 ± 0.02	20.93 ± 0.01	21.19 ± 0.04	21.11 ± 0.03	20.72 ± 0.04	20.98 ± 0.08
	G	0.00 ± 0.01	0.00 ± 0.01	20.67 ± 0.03	19.27 ± 0.02	18.67 ± 0.02	18.24 ± 0.02	18.04 ± 0.02
J1606–2333	A	−0.88 ± 0.01	0.30 ± 0.01	19.24 ± 0.01	19.11 ± 0.01	18.80 ± 0.01	18.88 ± 0.01	18.92 ± 0.05
	B	0.76 ± 0.01	−0.27 ± 0.01	19.42 ± 0.01	19.33 ± 0.01	18.99 ± 0.01	19.08 ± 0.02	19.12 ± 0.06
	C	−0.07 ± 0.01	−0.60 ± 0.01	19.79 ± 0.01	19.51 ± 0.02	19.22 ± 0.01	19.23 ± 0.02	19.27 ± 0.06
	D	0.24 ± 0.01	0.48 ± 0.01	20.23 ± 0.03	19.95 ± 0.03	19.46 ± 0.02	19.59 ± 0.02	19.66 ± 0.07
	G	0.00 ± 0.05	0.00 ± 0.05	21.67 ± 0.29	21.40 ± 0.25	20.85 ± 0.17	21.08 ± 0.29	19.75 ± 0.19

Table A1 – *continued*

	Component	α ('')	δ ('')	g	r	i	z	Y
J1640+1045	A	-0.37 ± 0.01	-0.36 ± 0.01	18.69 ± 0.01	18.73 ± 0.01	18.49 ± 0.01	18.28 ± 0.01	18.34 ± 0.01
	B	1.44 ± 0.01	0.92 ± 0.01	20.31 ± 0.01	20.34 ± 0.01	19.96 ± 0.01	19.89 ± 0.01	19.87 ± 0.01
	G	0.00 ± 0.01	0.00 ± 0.01	20.66 ± 0.04	19.25 ± 0.02	18.67 ± 0.01	18.66 ± 0.02	18.29 ± 0.02
J1709+3828	A	0.75 ± 0.01	-0.44 ± 0.02	21.49 ± 0.02	20.68 ± 0.01	20.70 ± 0.03	20.89 ± 0.05	21.29 ± 0.23
	B	-0.05 ± 0.01	1.06 ± 0.01	21.21 ± 0.01	20.65 ± 0.01	20.60 ± 0.02	20.91 ± 0.03	20.72 ± 0.07
	G	0.00 ± 0.02	0.00 ± 0.02	21.57 ± 0.04	20.06 ± 0.02	19.36 ± 0.02	18.98 ± 0.02	18.79 ± 0.03
J1710+4332	A	0.29 ± 0.01	1.67 ± 0.01	20.89 ± 0.01	21.09 ± 0.01	21.43 ± 0.01	21.20 ± 0.02	20.20 ± 0.02
	B	-0.17 ± 0.02	-0.72 ± 0.02	21.89 ± 0.01	21.99 ± 0.04	22.06 ± 0.07	21.34 ± 0.12	20.18 ± 0.15
	G	0.00 ± 0.05	0.00 ± 0.06	–	21.60 ± 0.08	20.60 ± 0.09	20.22 ± 0.09	20.38 ± 0.18
J1721+8842	A	-0.54 ± 0.01	-1.80 ± 0.01	19.45 ± 0.01	19.50 ± 0.02	19.14 ± 0.03	19.39 ± 0.02	19.14 ± 0.05
	B	-2.13 ± 0.01	-0.71 ± 0.01	20.57 ± 0.02	20.45 ± 0.02	20.18 ± 0.03	20.15 ± 0.03	19.88 ± 0.05
	C	1.88 ± 0.01	-1.10 ± 0.01	20.13 ± 0.01	20.04 ± 0.02	19.90 ± 0.03	19.91 ± 0.02	19.71 ± 0.05
	D	0.06 ± 0.02	1.69 ± 0.02	21.69 ± 0.04	21.43 ± 0.03	21.02 ± 0.05	21.18 ± 0.04	21.11 ± 0.08
	G	0.00 ± 0.01	0.00 ± 0.02	18.89 ± 0.02	18.47 ± 0.02	18.02 ± 0.03	17.97 ± 0.02	18.01 ± 0.04
J1831+5447	A	1.47 ± 0.01	1.10 ± 0.01	19.32 ± 0.01	19.14 ± 0.03	19.22 ± 0.02	19.08 ± 0.04	19.21 ± 0.06
	B	-0.37 ± 0.01	-0.27 ± 0.01	20.55 ± 0.03	20.07 ± 0.04	20.02 ± 0.03	19.58 ± 0.05	19.76 ± 0.08
	G	0.00 ± 0.02	0.00 ± 0.01	20.21 ± 0.07	18.95 ± 0.04	18.17 ± 0.01	17.76 ± 0.02	17.45 ± 0.03
J2124+1632	A	-0.04 ± 0.01	2.55 ± 0.01	18.99 ± 0.01	18.66 ± 0.01	18.80 ± 0.02	18.93 ± 0.03	19.08 ± 0.06
	B	0.13 ± 0.01	-0.46 ± 0.01	19.24 ± 0.02	19.16 ± 0.02	18.93 ± 0.03	19.34 ± 0.03	19.34 ± 0.08
	G	0.00 ± 0.01	0.00 ± 0.01	20.44 ± 0.10	18.88 ± 0.04	18.40 ± 0.04	18.03 ± 0.04	17.89 ± 0.05
J2305+3714	A	1.18 ± 0.01	-0.83 ± 0.01	17.96 ± 0.01	17.68 ± 0.01	17.34 ± 0.01	17.30 ± 0.01	17.28 ± 0.02
	B	-0.25 ± 0.01	0.84 ± 0.01	18.94 ± 0.01	18.99 ± 0.01	18.54 ± 0.01	18.51 ± 0.01	18.46 ± 0.02
	G	0.00 ± 0.02	0.00 ± 0.02	22.14 ± 0.43	18.59 ± 0.04	18.32 ± 0.03	18.05 ± 0.03	17.81 ± 0.05
J2332–1852	A	1.35 ± 0.01	0.43 ± 0.01	20.27 ± 0.01	20.24 ± 0.01	19.24 ± 0.01	19.68 ± 0.01	19.15 ± 0.01
	B	-0.43 ± 0.01	-0.41 ± 0.01	20.59 ± 0.01	20.59 ± 0.01	19.88 ± 0.03	20.21 ± 0.03	19.44 ± 0.03
	G	0.00 ± 0.02	0.00 ± 0.02	–	21.01 ± 0.05	18.93 ± 0.04	19.40 ± 0.04	18.71 ± 0.04

This paper has been typeset from a T_EX/L_AT_EX file prepared by the author.